In-Liquid Plasma-Mediated Manganese Oxide Electrocatalysts for Quasi-Industrial Water Oxidation and Selective Dehydrogenation

Indranil Mondal, Pramod V. Menezes, Konstantin Laun, Thomas Diemant, Mohammad Al-Shakran, Ingo Zebger, Timo Jacob, Matthias Driess, and Prashanth W. Menezes*

ABSTRACT: The production of renewable feedstocks through the coupled oxygen evolution reaction (OER) with selective organic oxidation requires a perfect balance in the choice of a catalyst and its synthesis access, morphology, and catalytic activity. Herein we report a rapid *in-liquid* plasma approach to produce a hierarchical amorphous birnessite-type manganese oxide layer on 3D nickel foam. The as-prepared anode exhibits an OER activity with overpotentials of 220, 250, and 270 mV for 100, 500, and 1000 mA·cm^{-2}, respectively, and can spontaneously be paired with chemoselective dehydrogenation of benzylamine under both ambient and industrial (6 M KOH, 65 °C) alkaline conditions. The in-depth *ex-situ* and *in-situ* characterization unequivocally demonstrate the intercalation of potassium in the birnessite-type phase with prevalent Mn^{III} states as an active structure, which displays a trade-off between porous morphology and bulk volume catalytic activity. Further, a structure−activity relationship is realized based on the cation size and structurally similar manganese oxide polymorphs. The presented method is a substantial step forward in developing a robust MnO$_x$ catalyst for combining effective industrial OER and value-added organic oxidation.

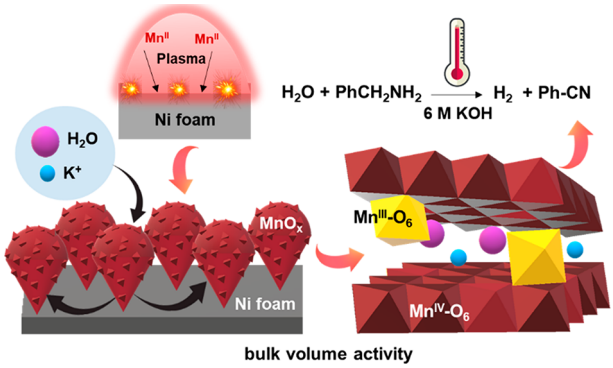

KEYWORDS: *water oxidation, organic transformation, manganese oxide, industrial activity, in-situ analysis*

INTRODUCTION

To establish a sustainable and greenhouse gas-free future, hydrogen (H_2) as a clean and high energy density feedstock has the potential to replace conventional fossil fuels.[1] In this regard, electrochemical water splitting allows the generation of pure H_2 (with the easily separable byproduct oxygen) and stores it without the use of a complicated assembly.[2,3] However, in the overall water splitting reaction, the rate of H_2 generation at the cathode largely depends on the kinetics of the oxygen evolution reaction (OER) at the anode, which involves energetically unfavorable four-electron consumption.[4] The HER kinetics can be accelerated either by introducing highly active OER catalysts or by replacing the OER process with the oxidation of protic organic compounds, which indeed decreases the required cell potentials dramatically and maximizes the energetic efficiency.[5−7] The overall reaction becomes economically more beneficial when a selective value-added oxidized product is generated instead of a low-value oxygen. However, to drive both OER and selective organic oxidation efficiently, developing active, stable (both mechanical and chemical), inexpensive, and earth-abundant electrocatalysts is essential and of utmost importance.[8]

Since the discovery of biological water oxidation associated with the photosystem II (PSII), Mn has gained significant attention as an OER central metal for artificial photosynthesis because of its suitable redox behavior in the catalytic process.[9−12] However, most of the commonly used synthetic Mn-oxide-based catalysts require a large overpotential to generate high OER current density and deactivate rather quickly under long-term assessment, making them industrially unsuitable as compared to other transition metal (e.g., Ni, Co, Fe) oxide catalysts. In OER, a layered birnessite-type MnO$_x$ structure with large interlayer distance, adequate edge sites,

stable Mn^{III} (with Jahn–Teller distortion), and short-range structure has a tremendous impact on the catalytic activity in the oxides.[10,13–21] Keeping this in mind, enormous efforts have been made over the past few years to synthesize numerous crystalline or amorphous layered MnO_x phases and monitor their *in-situ* reconstruction as well as understand the origin of the activity.

In addition to the catalyst's own properties, the choice of substrates and their adhesion to the catalyst strongly influence the overall activity.[22–24] In this context, nickel foam (NF) has recently received wide interest as a substrate due to its rigid and open porous network structure, mechanical strength, good electronic conductivity with a large surface area for electrochemical utilization, and favorable mass transport properties.[22] However, NF needs a suitable chemical binder or physical force to bind catalyst (powder) materials. To avoid this, lately, several binder-free techniques have been adopted;[25,26] however, most of them resulted in either low catalytic activity or instability of the catalyst layer at high current densities.

Compared to well-established synthetic approaches, the *in-liquid* (gas/liquid dual phase) plasma electrolytic oxidation (PEO) is a rapid, nontoxic technique that generates plasma glow discharge at the metal–electrolyte interface (MEI). Under high applied voltages, the PEO generates a harsh environment at the MEI (with a local temperature of 10,000 K and a pressure inside discharge channels of about 10^2–10^3 MPa).[27,28] Such conditions are indeed ideal to form a robust catalyst/substrate interface in the nanostructured anode that can overcome the persistent stability problem during intensive electrocatalytic oxidation ($V < 2.0$). Although PEO technique has been widely used for thin metal coatings,[29,30] its utilization to fabricate nanostructured anodes for electrocatalysis is relatively unexplored.

By taking advantage of the PEO technique, in this study, we considered addressing the following questions: (i) Is it possible to deposit manganese oxide with stabilized and prevalent Mn^{III} species using the *in-liquid* PEO technique? If so, (ii) can these electrodes be employed as active and stable anodes for the OER under an alkaline medium? (iii) Can the OER be replaced by multielectron organic oxidation? (iv) Would the anode material operate under ambient and industrially relevant reaction conditions (6 M KOH, 65 °C), and (v) what is the active structure and origin of the OER activity?

Herein, we report an industrially scalable and versatile *in-liquid* PEO approach that instantly forms nanostructured birnessite manganese oxide (MnO_x) films on a 3D NF surface. The produced MnO_x shows a porous hierarchical flower-like morphology that offers high catalytic surface area correlating with their superior electrocatalytic activity and stability toward the OER under both ambient and industrial relevant conditions. Furthermore, the active structure of the MnO_x electrodes has been comprehensively investigated by *in-situ* and *ex-situ* methods and determined to be a K-birnessite-type phase with stable Mn^{III} species. The role of the layered structure in this phase is elucidated by changing the intercalated cations, which along with structurally similar manganese oxide polymorphs helped to draw a structure–activity relationship and to understand deeper the origin of the OER activity. Notably, when OER is replaced by the dehydrogenation of benzylamine, value-added benzyl cyanide is formed selectively and a multifold enhancement in H_2 evolution occurs, demonstrating a promising technological advantage of the paired electrolysis.

RESULTS AND DISCUSSION

Fabrication of MnO_x Electrodes by PEO. The PEO anodic *in-situ* deposition was carried out at 630 V electrical charge on NF in the presence of 0.01 M $Mn(OAc)_2$ (OAc = acetate) using a simple two-electrode system as schematically depicted in Figure 1a (see the Experimental Section). During

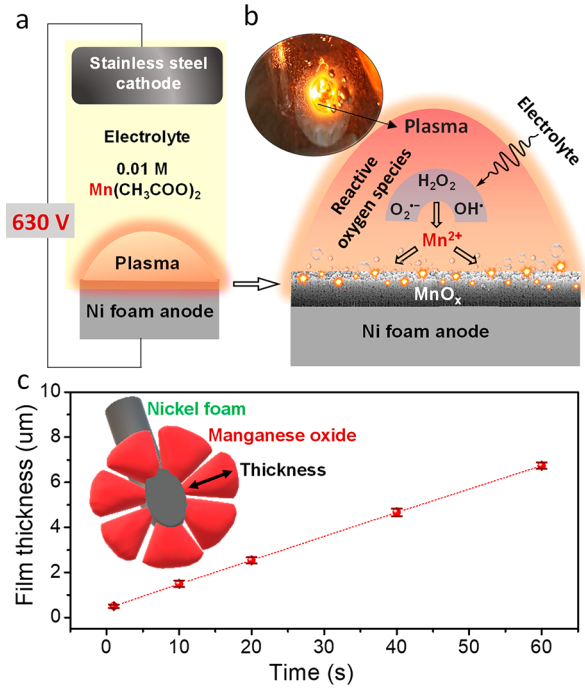

Figure 1. (a) Schematic diagram for the synthesis of MnO_x/NF using PEO; (b) demonstration of the MnO_x phase deposition involving reactive oxygen species originating from PEO (shown in inset) and (c) thickness variation of the MnO_x layer with PEO time. The graphical representation shows the hierarchical flower-like MnO_x nanostructure firmly embedded on NF.

high-energy PEO, transient reactive oxygen species ($O^{2\bullet-}$, $OH^\bullet$, H_2O_2) originate from the electrolyte and rapidly react with "free" Mn^{II} ions to deposit as manganese oxidic phase (MnO_x) onto the NF surface (Figure 1b).[31]

Interestingly, the scanning electron microscopy (SEM) investigations revealed the formation of hierarchical flower-like porous (defined in experimental section, SI) MnO_x structures within 1 s of plasma treatment (Figure S1). We further increased the PEO time to 10, 20, 40, and 60 s, and, in all cases, the newly formed MnO_x phase almost homogeneously covered the NF surface with retention of its morphology (Figures S2–S5). The thickness of the oxide layer was measured from an angular view of the SEM and was found to be linearly proportional to the PEO time (Figures 1c, S1–S5). A similar trend was observed for the accumulation of MnO_x mass (per cm^2) (Figure S6). Based on the OER activity (see later), we conducted further characterizations with only 40 s PEO-treated electrode. The focused ion beam (FIB) SEM and corresponding elemental mapping of the MnO_x/NF film cross-section confirmed that the MnO_x nanostructure was compactly embedded on the NF surface and ruled out any incorporation of Mn in the NF structure and *vice versa* (Figure 2).

The newly formed MnO_x phase was X-ray amorphous and composed of thin nanosheets that resemble well the previously

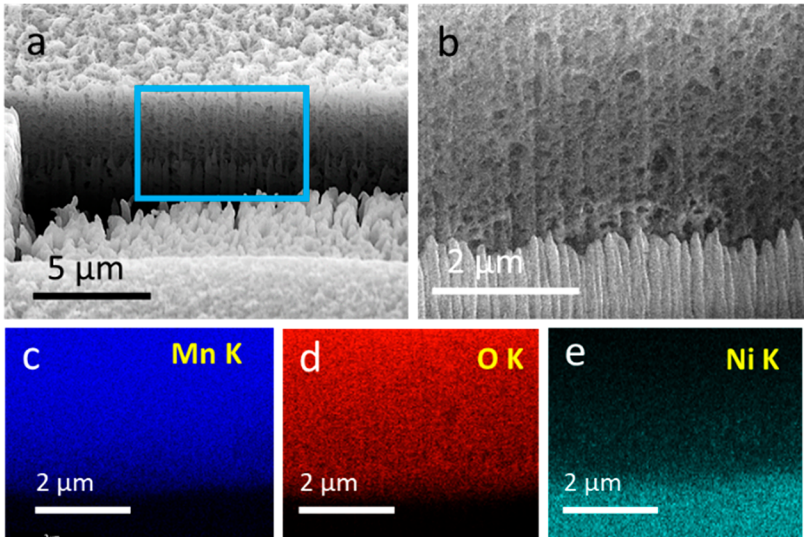

Figure 2. (a, b) SEM images (with different magnification) of a MnO_x/NF-40 specimen isolated with the FIB technique. (b) The region marked by a blue box in "panel a". (c, d, e) EDX elemental mapping for the Mn, O, and Ni.

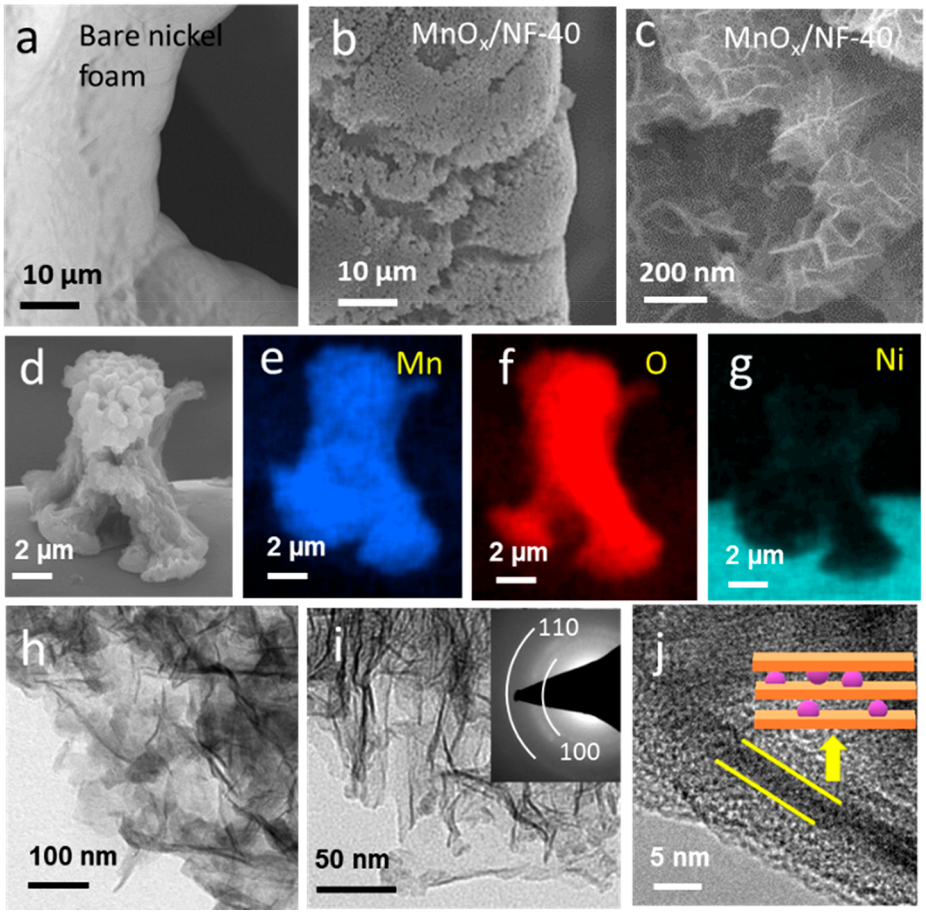

Figure 3. SEM image of (a) bare NF surface and (b, c) top view of MnO_x nanostructures on the NF surface that was synthesized with 40 s PEO (MnO_x/NF-40), showing an open porous structure of MnO_x. (d) Lateral view of a SEM image exhibiting free-standing MnO_x on an NF substrate. (e, f, g) SEM elemental mapping of Mn, O, and Ni extracted from the SEM image shown in panel d. (h, i, j) TEM image of MnO_x nanostructures with different magnifications. The inset of panel i displays the selected area electron diffraction (SAED) pattern extracted from MnO_x, which confirms to the (110) and (100) planes for birnessite-type MnO_x. Thin nanosheets of the MnO_x were observed in the TEM (panel j), and based on the measurement (2−5 nm), they may consist of several layered oxide units with intercalated species (typically observed for birnessite phase).

reported MnCat film (Figures 3, S7).[32,33] X-ray photoelectron spectroscopy (XPS) analysis confirmed the predominance of the $Mn^{III/IV}$ state accompanied by a slight Mn^{II} in the MnO_x phase (Figure S8). The Mn to O atomic ratio calculated using

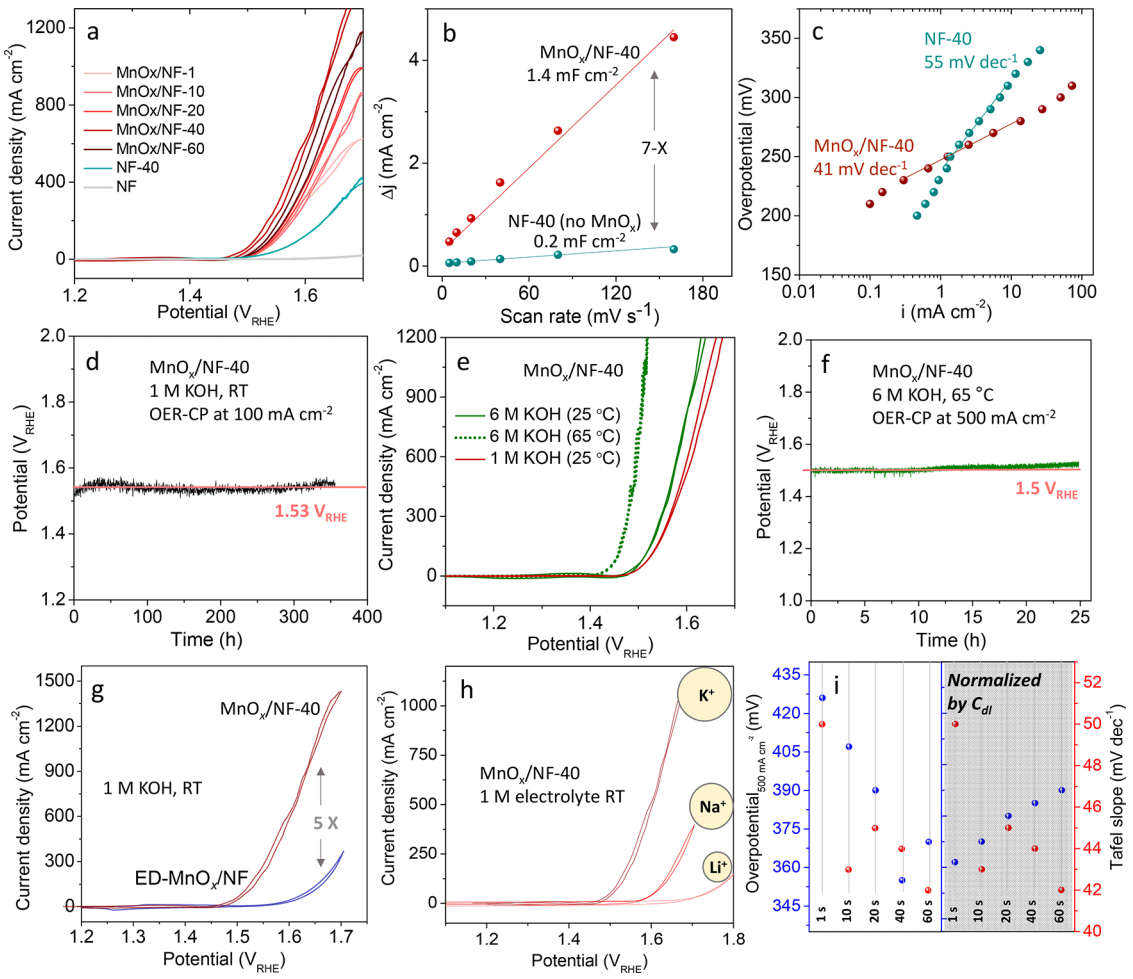

Figure 4. (a) CVs of MnO_x/NF electrodes at a scan rate of 2 mV s^{-1} and (b) C_{dl} values extracted from an analysis of CVs with varying scan rates of MnO_x/NF-40 and NF-40 electrodes in the non-Faradaic region. (c) Tafel plot of the MnO_x/NF-40 electrode obtained from steady-state measurements. (d) OER-CP at 100 mA·cm^{-2}. (e) CVs of MnO_x/NF-40 electrodes at industrially relevant elevated temperature and electrolyte concentration. (f) OER-CP at 500 mA·cm^{-2} with the MnO_x/NF-40 anode. (g) Comparison of CV current density between electrodeposited (ED-MnO_x/NF) and plasma-mediated MnO_x/NF (MnO_x/NF-40) electrodes. (h) CV curve recorded in a different electrolyte solution (LiOH, NaOH, and KOH) shows the activity increases with the size of the cation present in the electrolyte. (i) C_{dl} normalized CV and steady-state current density (measured with chronoamperometry) value recorded at different potentials for normalized Tafel measurements. At the bottom of panel i, PEO times are mentioned.

SEM energy dispersive X-ray spectroscopy (EDX) was 1:1.6 (Figure S9). Further investigation on the morphology, surface, and bulk composition of the MnO_x/NF films was carried out by SEM, transmission electron microscopy (TEM) coupled with EDX, and XPS depth profiling (Figure 3, Figures S8–S11), and the attained results for the as-prepared MnO_x phase closely matched the previously reported hydrated birnessite-type structure.[12,34]

Electrochemical OER. The electrocatalytic OER activity of MnO_x/NF films was measured in an aqueous 1 M KOH solution at room temperature (RT) using a standard three-electrode setup. Depending on the PEO treatment time (1, 10, 20, 40, 60 s), the electrodes were named as MnO_x/NF-1, -10, -20, -40, and -60, respectively. Before evaluation of the OER activities, the electrodes were activated using cyclic voltammetry (CV) in the range 1−1.5 V_{RHE} until a stable current response was achieved (Figure S12). Furthermore, electrodeposited manganese oxide and PEO-treated NF without $Mn(OAc)_2$ (NF-40) were synthesized as the control anodes to compare the activity and understand the structure−activity relationship (Figures S13−S15). The electrodeposited manganese oxide (ED-MnO_x/NF) is also X-ray amorphous as well as structurally and electronically similar to the plasma-derived MnO_x (Figures S13, S14). Taking a closer look, the selected MnO_x/NF-40 exhibited multiple redox peaks in the region of 1.1−1.4 V_{RHE}, indicating the transformation of the valence state of Mn from lower (Mn^{II}/Mn^{III}) to higher (Mn^{III}/Mn^{IV}), which was clearly distinguishable from a typical Ni^{II}/Ni^{III} couple observed for NF-40 (Figure S12). The CV measurements showed that MnO_x/NF-40 has the optimum activity among all PEO-treated electrodes, and the overpotentials (η) of this anode required to reach the current density values of 100 and 500 mA·cm^{-2} were merely 280 and 350 mV (±10 mV), respectively (Figure 4a). The overpotential obtained here for MnO_x/NF-40 is the lowest compared to the previously reported MnO_x catalysts in alkaline media as well as superior to most of the transition-metal-based electrodes reported to date (Tables S1, S2). The catalytic activity was well correlated with the double layer capacitance (C_{dl}) values extracted from CVs in the non-Faradaic region (Figures S16, S17), which is proportional to the electrochemically active surface area (ECSA).[35] Within the PEO-treated electrodes, MnO_x/NF-40

displayed the highest C_{dl}, which was even 7-fold higher as compared to the NF-40 (Figure 4b). The Tafel slope was estimated from the linear region of the steady-state Tafel plots. A small slope value for MnO_x/NF-40 (41 mV·dec^{-1}) was observed as compared to NF-40. A considerably similar slope value for all PEO-treated MnO_x/NF electrodes implies that they have the same kind of active sites and the OER rate-limiting step,[36,37] and are most likely associated with the second electron transfer unlike NF-40 (Figures 4c, S18).[38] Besides, the charge transfer resistance (R_{ct}) for all PEO-treated catalysts was extracted from Nyquist plots in the electrochemical impedance spectra (Figure S19, Table S3) and is in line with the activity of the MnO_x/NF films.

Another key activity parameter in electrocatalysis is the durability of the catalyst under the operating conditions. It has often been shown in the literature that MnO_x-based catalysts usually fail to generate current densities of even 10 mA·cm^{-2} with deteriorating stability. We further chose our most active MnO_x/NF-40 electrode and performed long-term chronopotentiometry (CP) tests at a current density of 100 mA·cm^{-2}. The result indicated no significant activity drop over 350 h (Figure 4d). Encouraged by this result, we applied the same electrode in industrially relevant conditions, i.e., 6 M KOH at 65 ± 1 °C. The recorded CV of the MnO_x/NF-40 film displayed a multifold enhancement in current density, reaching more than 1000 mA·cm^{-2} at 1.5 V_{RHE} (Figure 4e).[39] Subsequently, the OER-CP was conducted at a current density of 500 mA·cm^{-2} (Figure 4f) for more than 24 h, and no significant activity drop was observed, implying its potential for practical applications. It is worth noting that at 6 M KOH the CV current density and Tafel slope linearly change with temperature, which implies that the water oxidation pathway and rate-determining steps did not alter (Figure S20). We further investigated the activity comparison between electrodeposited and PEO-mediated MnO_x, which is structurally and electronically similar. Interestingly, an almost 5-fold higher activity was observed for the plasma sample (Figure 4g). Moreover, to find the impact of an electrolyte cation on the birnessite layered structure, we tested the plasma sample under different electrolyte media, namely, LiOH, NaOH, and KOH. The activity increased with the size of the cation in the order of K^+ > Na^+> Li^+ (Figure 4h). This is consistent with the previously reported results.[40] The present observation helped to build a structure−activity relationship, which is discussed in the latter section. Furthermore, to compare the OER activity of MnO_x/NF with benchmark catalysts, we deposited commercial IrO_2 and different manganese oxide polymorphs on NF using a chemical binder-free electrophoretic deposition technique with a similar loading amount (0.8 mg·cm^{-2}). The LSVs measured under industrial conditions also confirmed a higher OER activity of MnO_x/NF-40 in comparison to those of other commercial catalysts (Figure S21).

Post-OER *ex-Situ* Analysis. To find the origin of the OER activity of the MnO_x/NF-40 electrode, extensive *ex-situ* characterizations were conducted. SEM images of the MnO_x/NF-40 film after OER-CP (100 mA·cm^{-2}) at ambient conditions indicated that MnO_x nanostructures are mechanically stable, as they are strongly adhered to and homogeneously covered the NF surface (Figure S22). Importantly, the post-OER MnO_x was also X-ray amorphous, similar to that of the as-prepared sample (Figure S23). Moreover, we sonicated the film in acetone to peel off a portion of MnO_x nanostructures and recorded the SEM-EDX and elemental mapping of both the film and residual particles (Figures S24, S25). The result showed homogeneous incorporation of potassium (K) (almost 3%) throughout the MnO_x nanostructures. Similarly, we observed the incorporation of Li and Na in the MnO_x layer (Figures S26, S27). Moreover, the TEM image of the particles after the OER displayed a fine, porous morphology similar to that of the as-prepared MnO_x (Figure S28). Interestingly, a closer look at the morphology revealed ordered layers of crystallites located discretely over the nanostructures. After OER, a large interlayer distance of 7.2 Å unequivocally confirmed the expansion of interlayer distances due to K incorporation between oxo layers (Figures 5a, S29),[40] and the inverse fast Fourier transform (FFT) image

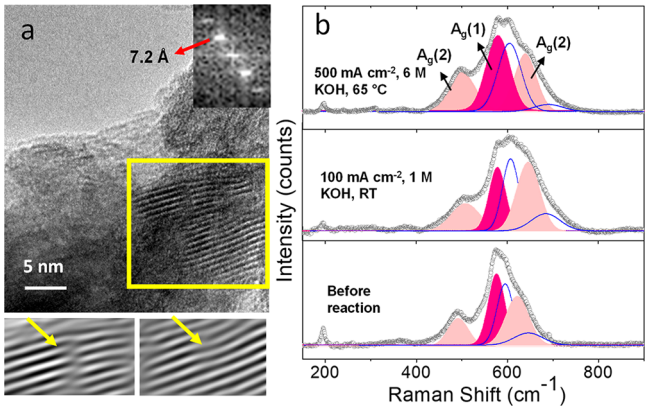

Figure 5. (a) TEM image of post-OER (OER-CP at 100 mA·cm^{-2} in 1 M KOH, RT) MnO_x/NF-40. The inset shows the FFT profile extracted from the yellow marked area. The bottom images are the inverse projection of the FFT profile extracted from the same area, and the yellow arrows indicate the line defects in the crystallites. (b) Quasi *in-situ* Raman spectra of MnO_x/NF-40. In addition to the $A_g(1)$ and $A_g(2)$ bands, two additional peaks at around 600 and 700 cm^{-1} were also observed in the birnessite phase and can be assigned to the stretching vibrations and degree of polymerization of [Mn-O_6] units.[14,47]

clearly indicated the presence of line defects within the crystallite domains (Figures 5a, S29) that were not observed before OER.[41] A similar feature was also observed for the industrially driven OER-CP electrode (500 mA·cm^{-2}) except for a slightly higher incorporation of K (5%) (Figures S30−S32). Overall, the hierarchical porous morphology of the MnO_x nanostructure after the OER remained unaltered and did not depend on the OER condition (Figrue S33). XPS was recorded to investigate the surface chemical state of the MnO_x after the OER. The spectral shape of the Mn 2p under both ambient and industrial conditions confirms no significant difference. The mixture of $Mn^{III/IV}$ species persists, and a slight Mn^{II} oxidation was unavoidable in the MnO_x during the OER (Figure S34). The O 1s spectra display two characteristic peaks, one at 529.9 eV responsible for O^{2-} from Mn−O bonds and the other at 531.3 eV related to hydroxylated Mn (Figure S34).[42]

Further, the surface and subsurface oxidation state of Ni was also measured to track any changes on NF after the OER. The PEO treatment slightly modified the NF surface and weakened the Ni^0 signal (at 852.6 eV), which confirms the formation of Ni-oxo species. After OER, the Ni^0 was absent and only $Ni^{II/III}$ species were visible (with a peak maximum at 855.5 eV) (Figure S35).[43,44] This surface-hydrated nickel oxide might

also contribute to the OER activity of MnO_x; however, as the PEO reference NF-40 under identical conditions did not show any considerable activity, we possibly could rule out its major contribution.[45,46]

Quasi *in-Situ* Raman Spectroscopy. As the vibrations in the oxidic polymorphs of manganese are Raman responsive, we aimed to elucidate the dynamic self-reconstruction and structure of the catalytically active phase of the as-prepared MnO_x using quasi *in-situ* Raman analysis (Figure 5b). The Raman spectrum before OER of the MnO_x/NF-40 film displayed multiple peaks in the region of 400−700 cm^{-1}, in which three dominant marker bands are present, typically observed for δ-MnO_2, a layered polymorph majorly containing a mixed $Mn^{III/IV}$ valence state.[20,48] The Raman band centered around 578 cm^{-1} corresponds to an in-plane Mn−O stretching vibration ($A_g(1)$) along the octahedral layers in δ-MnO_2, while the two other peaks at ∼500 and ∼645 cm^{-1} are associated with out-of-plane Mn−O vibrations ($A_g(2)$) perpendicular to the layers.[20,48,49] All three bands, along with a lower frequency phonon (LFP) band at around 198 cm^{-1}, are correlated with the oxidation states of Mn in the [Mn-O_6] unit, the interlayer separation between the oxo-domains, and structural distortions of the involved Mn−O environments in birnessite-type MnO_x.[14,47] Interestingly, after OER (at both ambient and industrial conditions) the higher frequency $A_g(2)$ band intensity increased, while the LFP band intensity at 198 cm^{-1} decreased, which implies the formation of a K-birnessite-type structure.[14,47]

The formation of the K-birnessite-type structure and its dynamic self-reconstruction were further verified by potential-dependent *in-situ* Raman analysis on the MnO_x/NF-40 film under ambient conditions (Figure S36). The results clearly exhibited a monotonic shift of the $A_g(2)$ bands with a gradual increase of the potential from 1.2 to 1.7 V_{RHE}. This suggests that the intercalation of K between Mn-oxo layers is also potential-dependent. Thus, it is worth noting that, during the OER, the MnO_x film still preserved the layered structure probably with lower long-range order, higher strain, and more defects, caused by the K intercalation and oxidation state change. To understand the NF surface structure and MnO_x nanostructures, Raman spectra were acquired on a sample from which a part of the MnO_x nanostructures was removed. The spectra revealed the formation of NiOOH with its characteristic vibrations for the depolarized δ-mode and polarized ν-mode from the Ni−O bond in [Ni^{III}-O_6] units (Figure S37).[45,46,50]

A General Model for OER Active Structure. From the in-depth *ex-situ* and *in-situ* analysis results, we conclude that a porous hierarchical nanostructured birnessite-type MnO_x was formed under the PEO treatment, which was X-ray amorphous. Upon the onset of the OER, the morphology and the structure of MnO_x apparently remained intact except for the incorporation of K in the structure and a slight change in the Mn oxidation state. K is incorporated as K^+ ion channelizing through the electrolyte and reaches in between Mn-oxo layers to neutralize the uncompensated negative charges.[40] A similar phenomenon occurred with Li and Na incorporation. Keeping this in mind, the higher activity of the generated MnO_x nanostructure can primarily be ascribed to the porous morphology resulting in a large surface area (C_{dl} value) combined with the bulk (volume) activity that allows the electrolyte to penetrate through the porous structure deep inside the film close to the NF/MnO_x interface.[51] The activity difference among PEO MnO_x/NF electrodes is mainly caused by the number of redox-active centers, which differs with a varied layer thickness (or mass) of the catalyst. Since the C_{dl} value of a catalyst layer reflects its bulk (volume) activity,[51] the origin of the catalytic activity was tracked by normalizing the CV current response by C_{dl}, which resulted in a similar current density value with no clear trends in the polarization curve (Figure 4i). Additionally, the Tafel slope measured after normalizing the steady-state current with C_{dl} concludes that the rate-determining step is independent of the film thickness (Figure 4i).[52] This is certainly advantageous because a large number of oxy-cations (mostly Mn from MnO_x and maybe also a lower amount of Ni from NF) can be involved in the OER.[53] In addition to the morphology of the film, the oxidation state and structure of the Mn-oxo clusters have a tremendous impact on the OER. It is well known that the active structure for MnO_x comprising K-birnessite-type polymorphs with stable and prevalent Mn^{III} species (Figure 6) is active for OER. The intercalation of K and water

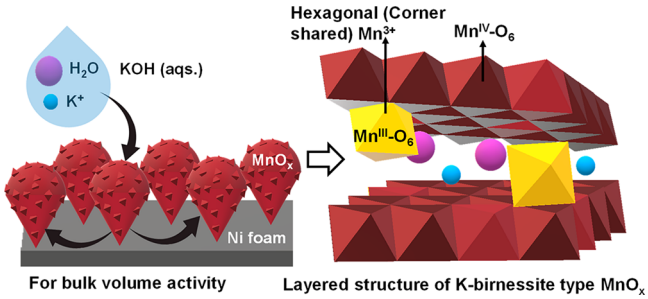

Figure 6. Schematic illustration of the bulk volume activity of MnO_x/NF during alkaline water oxidation. Due to the highly porous nature of MnO_x, the electrolyte percolates through MnO_x layers and enters deeply inside near the MnO_x/NF interface (shown with black arrows). The pictorial representation shows that the active structure is the K-birnessite-type MnO_x with intercalated K^+ and H_2O molecules between layered Mn-oxo crystallites.

molecules could be decisive to allow more Mn centers to be exposed to the electrolyte by increasing the interlayer spacing, favoring the formation of small domains that stack in an unordered fashion and can contain a higher number of edge sites.[54−58] This has been further validated by the reduced activity with a smaller cation size. K^+, with the maximum ionic radius, causes larger inlayer spacing and thus tends to show more bulk (volume) activity as compared to Li^+. Interestingly, not all K-birnessite-type structures are OER-active. The post-OER electrodeposited MnO_x film (ED-MnO_x/NF) also displayed homogeneous K incorporation in the MnO_x layer; however, it failed to show a similar activity to that for PEO-derived MnO_x/NF electrode (Figure S38). The result concludes that a compact and dense morphology is not beneficial for the OER. Overall, the OER-active K-intercalated birnessite-type MnO_x comprises a homogeneous porosity with an increased electrochemical surface area that further results in deep electrolyte penetration and bulk volume activity, lower charge transfer resistance, fast-redox switchability, short-range order, small oxo domains that expose more edge sites containing the mixed Mn^{III}/Mn^{IV} valence state with a large number of μ-oxo bridged structures, and plenty of water/proton exchange sites to facilitate the O_2 evolution. This observation is consistent with the proposed OER reaction

mechanisms for the previously reported manganese oxide catalysts in an alkaline medium.[14,16,59] We further conclude that the nature of the active structure (K-birnessite) is stable under both ambient and industrial conditions, and importantly, abundant active Mn^{III} did not convert into inactive Mn^{IV} states during the OER. The stability of Mn^{III} can also partially be assisted by the slow disproportionation of Mn^{III} into Mn^{IV} and Mn^{II} ions within the alkaline medium.

Electrooxidation of Benzylamine. To examine the practical viability of the as-prepared MnO_x/NF anode, we replaced the OER reaction with the electrochemical dehydrogenation of benzylamine (BA). This reaction offers a double advantage by utilizing BA as a proton-donating agent for accelerating H_2 production at the cathode and production of benzyl cyanide (BC) as a value-added chemical, an important intermediate for the synthesis of pharmaceuticals and pesticides, at the anode.[46,60]

The oxidation of BA (50 mM) was carried out in both ambient and industrial conditions (Figure 7a). The LSV curve

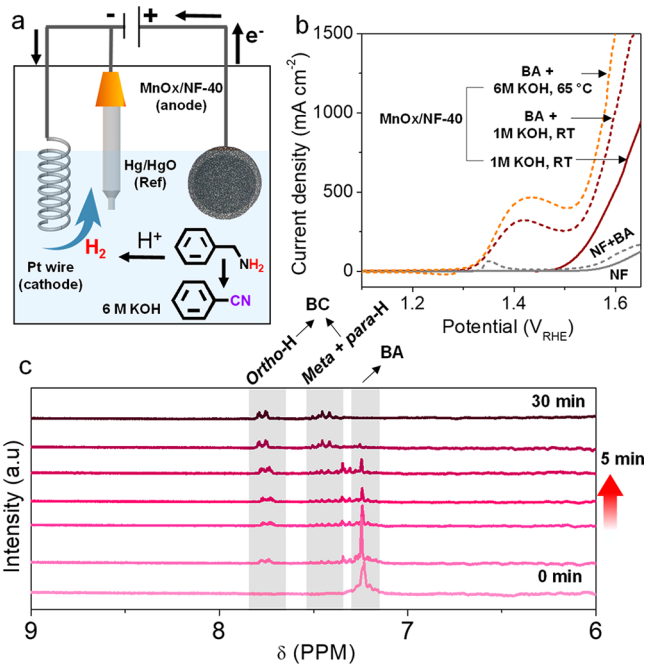

Figure 7. (a) Schematic representation for the dehydrogenation of benzylamine coupled with cathodic hydrogen evolution in an undivided cell. (b) LSV recorded at a scan rate of 2 mV s^{-1} with MnO_x/NF-40 and bare NF in the presence of 50 mM benzylamine solution (10 mL of 1 M KOH). (c) Temporal plot for the ^1H NMR analysis recorded with solution after bulk electrolysis at ambient condition. The result indicated a full product formation within 30 min of the reaction. For bulk electrolysis and ^1H NMR under industrial conditions, see Figures S39, S40.

displayed a broad redox feature starting from 1.35 V_{RHE} followed by a steep rise in the OER region, with the current density value reaching 1000 mA·cm^{-2} at 1.6 and 1.56 V_{RHE} under ambient and industrial conditions, respectively (Figure 7b). The bulk electrolysis at 1.5 V_{RHE} confirms that the oxidation of BA is associated with a high anodic current density (30 times higher than the current of the OER), which gradually decreased with the consumption of BA (Figure 7c). We deliberately choose this potential to confirm that all the redox-active Mn centers transformed into higher valent Mn (e.g., III or IV) with minimum OER activity. The consumption of BA and the formation of BC were monitored with successive ^1H NMR spectra of the reaction solution (Figure S30). The full conversion of BA to BC was observed within 30 and 20 min under ambient and industrial conditions, respectively (Figures 7c, S39). In both cases, the charge transfer quantity was almost 190 C. The ^1H NMR spectra further confirmed that no organic intermediate was detected during bulk electrolysis (Figure 7c). The BA to BC conversion and corresponding Faradaic efficiency (FE) were calculated to be 99 ± 5% under both conditions. The FE was calculated based on the charge consumed for 99% conversion of BA to BC (equivalent to 188 C). Bare NF is poorly active, and the conversion did not reach 50% after 30 min of electrolysis. The dehydrogenation of BA may follow a multistep pathway similar to that of alcohol oxidation.[61] Briefly, it can undergo H^- transfer via highly reactive imine intermediate formation. In the H^- transfer step, $Mn^{III}Mn^{IV}$-oxo species regenerate, which takes part in the proton-coupled electron transfer process in the further course of the reaction (details in Scheme S1).[36] In order to investigate the influence of BA oxidation on the H_2 production yield, we performed additional bulk electrolysis in a H-cell setup. After 30 min of the electrolysis, we estimated almost 76 vol % of H_2 evolution, caused by the BA oxidation. The H_2 production yield is well correlated with the mechanistic pathway. These results suggest that the herein-presented organic oxidation replacing anodic OER is an atom and energy economic process (Figure S41).

CONCLUSION

Using a nontoxic, inexpensive, thermal glow discharge, *in-liquid* PEO technique, the rapid, *in-situ* growth of birnessite-type manganese oxide can be achieved on nickel foams. The as-synthesized manganese oxide is porous and hierarchical with flower-like nanostructures that lead to an increase in surface area and the accessible number of active sites for anodic water oxidation. Using this MnO_x/NF film for the OER, a high anodic current density of 500 mA·cm^{-2} could be achieved at 1.5 V_{RHE} under industrially relevant conditions (6 M KOH, 65 °C), and no activity decrease could be observed for almost 350 h at 100 mA/cm^2. Further, using the MnO_x/NF, the water oxidation can be replaced by the electrocatalytic dehydrogenation of benzylamine, which accomplished selective production of benzyl cyanide with an elevated anodic current density up to 1000 mA·cm^{-2} at 1.5 V_{RHE}. The electrodes obtained showed an unaffected morphology even at strongly anodic catalytic conditions, as presumed since they were invigorated with much harsher adapted conditions during the synthesis. The birnessite MnO_x showed structurally and electronically a slight change during electrocatalysis except for the incorporation of K. The catalytic activity was primarily governed by the stable and prevalent Mn^{III} sites, short-range structure, and porous morphology, which assisted the increased terminal ligation of the water molecule and bulk volume activity to access more redox-active centers, although a minor contribution from the NF surface cannot be completely ruled out.

EXPERIMENTAL SECTION

Plasma Electrolysis. PEO was conducted by using a TDK-Lambda programmable DC power supply (GEN600-1.3/E, 1U, 780W, RS-232/RS-485). A LabVIEW software (National Instruments) was used to control the power supply and record the voltage and current data electronically. Electrolysis was carried out in a

double-walled glass cell with a volume of 300 mL, equipped with magnetic stirring and a water-cooling system to maintain the electrolyte temperature in the range 30−45 °C. Stainless steel with dimensions of 20 × 20 × 2 mm was used as a counter electrode (cathode), and NF served as the working electrode (anode). Prior to the electrolysis, the NF electrodes were first prepared and sonicated in 85% phosphoric acid (Merck) for 1 min to remove organic contaminants and the native oxide layer from the surface followed by thoroughly rinsing with ultrapure water (18.2 MΩ cm, TOC ≤ 3 ppb) and drying in air before use. A polypropylene tip was used on both sides of the NF substrate to define the treatment area and obtain a homogeneous electric field during electrolysis. The distance between the cathode and anode was maintained at 50 mm. A 200 mL amount of a 0.01 M $Mn(OAc)_2$ (≥99%, Sigma-Aldrich) solution was used as the electrolyte, which was prepared using ultrapure water (18.2 MΩ cm, TOC ≤ 3 ppb). PEO was performed using a constant 630 V with different times ranging from 1 to 60 s. An intense plasma glow discharge was visible during the PEO process. After the experiment, the prepared electrodes were thoroughly rinsed with ultrapure water and dried in an N_2 gas flow. In order to simplify the sample description, we have denoted the PEO-derived samples as "MnO_x/NF-PEO time". For example "MnO_x/NF-40" is the MnO_x/NF film prepared using a 40 s PEO treatment. As a reference sample, we used NF-40, which was prepared using 40 s of PEO treatment without $Mn(OAc)_2$. The plasma-treated area is circular with a diameter of 5 mm in the center of the NF substrate. For electrocatalytic measurements, the untreated edges were cut off.

Electrocatalytic Measurements. The typical electrochemical activities were measured using a standard three-electrode (working, counter, and reference) system with a potentiostat (SP-200, BioLogic Science Instruments) controlled by the EC-Lab version 10.20 software package. A commercial 1 M aqueous KOH solution was used as the electrolyte. The PEO-driven and as-deposited catalysts on NF served as the working electrodes, Pt wire (0.5 mm diameter × 230 mm length; A-002234, BioLogic) as a counter, and Hg/HgO as the reference electrode (CH Instruments, Inc.). CV and LSV were carried out with an applied *iR* compensation of 80% with a scan rate of 2 mV s^{-1}. The potentials presented in this work were referenced to the reversible hydrogen electrode (RHE) through calibration and in 1 M aqueous KOH, $E(RHE) = E(Hg/HgO) + 0.098\ V + (0.059 \times pH)\ V$. The details of Tafel, ECSA, EIS, and temperature-dependent potential calibration measurements are described in the Supporting Information.

Electrooxidation of Benzylamine. The linear sweep voltammetry and bulk electrolysis were performed in a three-electrode setup analogously to one of the other OER studies. The PEO-mediated MnO_x/NF electrode was directly used as the anode and a platinum wire as the cathode in a 50 mM amine solution containing 10 mL of 1 M purified KOH solution. For bulk electrolysis, the CA experiment was performed at 1.5 V_{RHE}.

AUTHOR INFORMATION

Corresponding Author

Prashanth W. Menezes − *Department of Chemistry: Metalorganics and Inorganic Materials, Technische Universität Berlin, 10623 Berlin, Germany; Materials Chemistry Group for Thin Film Catalysis−CatLab, Helmholtz−Zentrum Berlin für Materialien und Energie, 12489 Berlin, Germany;* orcid.org/0000-0002-0665-7690; Email: prashanth.menezes@helmholtz-berlin.de, prashanth.menezes@mailbox.tu-berlin.de

Authors

Indranil Mondal − *Department of Chemistry: Metalorganics and Inorganic Materials, Technische Universität Berlin, 10623 Berlin, Germany;* orcid.org/0000-0003-4543-0058

Pramod V. Menezes − *Institute of Electrochemistry, Ulm University, 89081 Ulm, Germany*

Konstantin Laun − *Department of Chemistry: Physical Chemistry/Biophysical Chemistry, Technische Universität Berlin, 10623 Berlin, Germany*

Thomas Diemant − *Helmholtz-Institute Ulm−Electrochemical Energy Storage, 89081 Ulm, Germany; Karlsruhe Institute of Technology, 76021 Karlsruhe, Germany*

Mohammad Al-Shakran − *Institute of Electrochemistry, Ulm University, 89081 Ulm, Germany*

Ingo Zebger − *Department of Chemistry: Physical Chemistry/Biophysical Chemistry, Technische Universität Berlin, 10623 Berlin, Germany;* orcid.org/0000-0002-6354-3585

Timo Jacob − *Institute of Electrochemistry, Ulm University, 89081 Ulm, Germany; Helmholtz-Institute Ulm−Electrochemical Energy Storage, 89081 Ulm, Germany; Karlsruhe Institute of Technology, 76021 Karlsruhe, Germany;* orcid.org/0000-0001-7777-2306

Matthias Driess − *Department of Chemistry: Metalorganics and Inorganic Materials, Technische Universität Berlin, 10623 Berlin, Germany;* orcid.org/0000-0002-9873-4103

Author Contributions

I.M. and P.V.M. contributed equally to this work (synthesis, electrochemical experiment, SEM, TEM, data interpretation, and writing the manuscript). K.L. and I.Z. measured the *in-situ* Raman spectra, and T.D. and A.S. performed the XPS and SEM-FIB analysis, respectively. T.J. and M.D. helped to provide resources and analysis and interpretation of the analytical data. P.W.M. conceived the idea, designed the work, supervised the project, and co-wrote/edited the manuscript.

Notes

The authors declare no competing financial interest.

ACKNOWLEDGMENTS

This work was funded by the Deutsche Forschungsgemeinschaft (DFG, German Research Foundation) under Germany's Excellence Strategy−EXC 2008−390540038−UniSysCat and the German Federal Ministry of Education and Research

(BMBF project "PrometH2eus", 03HY105C). P.W.M. greatly acknowledges support from the German Federal Ministry of Education and Research in the framework of the project Catlab (03EW0015A/B). T.J. and P.V.M. gratefully acknowledge support by the DFG through the collaborative research center SFB-1316 (Project ID: 327886311) as well as the state of Baden-Württemberg and the DFG through Grant No. INST 40/574-1 FUGG. I.M. is indebted to Alexander von Humboldt Stiftung for the postdoctoral fellowship. The authors are grateful to J. N. Hausmann for the TEM analysis. K.L. acknowledges the Einstein Foundation Berlin for funding in the framework of the Einstein Center of Catalysis (EC^2)/BIGNSE.

REFERENCES

(1) van Renssen, S. The Hydrogen Slution? *Nat. Clim. Chang.* **2020**, *10*, 799−801.

(2) Luo, Y.; Zhang, Z.; Chhowalla, M.; Liu, B. Recent Advances in Design of Electrocatalysts for High-Current-Density Water Splitting. *Adv. Mater.* **2022**, *34*, 2108133.

(3) Yang, F.; Kim, M. J.; Brown, M.; Wiley, B. J. Alkaline Water Electrolysis at 25 A Cm^{-2} with a Microfibrous Flow-through Electrode. *Adv. Energy Mater.* **2020**, *10*, 2001174.

(4) Liang, Q.; Brocks, G.; Bieberle-Hütter, A. Oxygen Evolution Reaction (OER) Mechanism under Alkaline and Acidic Conditions. *J. Phys. Energy* **2021**, *3*, 026001.

(5) Li, Y.; Wei, X.; Chen, L.; Shi, J. Electrocatalytic Hydrogen Production Trilogy. *Angew. Chemie Int. Ed.* **2021**, *60*, 19550−19571.

(6) Hausmann, J. N.; Menezes, P. V.; Vijaykumar, G.; Laun, K.; Diemant, T.; Zebger, I.; Jacob, T.; Driess, M.; Menezes, P. W. In-Liquid Plasma Modified Nickel Foam: NiOOH/NiFeOOH Active Site Multiplication for Electrocatalytic Alcohol, Aldehyde, and Water Oxidation. *Adv. Energy Mater.* **2022**, *12*, 2202098.

(7) Hausmann, J. N.; Beltrán-Suito, R.; Mebs, S.; Hlukhyy, V.; Fässler, T. F.; Dau, H.; Driess, M.; Menezes, P. W. Evolving Highly Active Oxidic Iron(III) Phase from Corrosion of Intermetallic Iron Silicide to Master Efficient Electrocatalytic Water Oxidation and Selective Oxygenation of 5-Hydroxymethylfurfural. *Adv. Mater.* **2021**, *33*, 2008823.

(8) Kahlstorf, T.; Hausmann, J. N.; Sontheimer, T.; Menezes, P. W. Challenges for Hybrid Water Electrolysis to Replace the Oxygen Evolution Reaction on an Industrial Scale. *Glob. Challenges* **2023**, 2200242.

(9) Wiechen, M.; Najafpour, M. M.; Allakhverdiev, S. I.; Spiccia, L. Water Oxidation Catalysis by Manganese Oxides: Learning from Evolution. *Energy Environ. Sci.* **2014**, *7*, 2203−2212.

(10) Zaharieva, I.; González-Flores, D.; Asfari, B.; Pasquini, C.; Mohammadi, M. R.; Klingan, K.; Zizak, I.; Loos, S.; Chernev, P.; Dau, H. Water Oxidation Catalysis − Role of Redox and Structural Dynamics in Biological Photosynthesis and Inorganic Manganese Oxides. *Energy Environ. Sci.* **2016**, *9*, 2433−2443.

(11) Zhang, C.; Chen, C.; Dong, H.; Shen, J.-R.; Dau, H.; Zhao, J. A Synthetic Mn_4Ca-Cluster Mimicking the Oxygen-Evolving Center of Photosynthesis. *Science* **2015**, *348*, 690−693.

(12) Post, J. E. Manganese Oxide Minerals: Crystal Structures and Economic and Environmental Significance. *Proc. Natl. Acad. Sci. U. S. A.* **1999**, *96*, 3447−3454.

(13) Walter, C.; Menezes, P. W.; Orthmann, S.; Schuch, J.; Connor, P.; Kaiser, B.; Lerch, M.; Driess, M. A Molecular Approach to Manganese Nitride Acting as a High Performance Electrocatalyst in the Oxygen Evolution Reaction. *Angew. Chemie Int. Ed.* **2018**, *57*, 698−702.

(14) Menezes, P. W.; Walter, C.; Chakraborty, B.; Hausmann, J. N.; Zaharieva, I.; Frick, A.; Hauff, E.; Dau, H.; Driess, M. Combination of Highly Efficient Electrocatalytic Water Oxidation with Selective Oxygenation of Organic Substrates Using Manganese Borophosphates. *Adv. Mater.* **2021**, *33*, 2004098.

(15) Walter, C.; Menezes, P. W.; Loos, S.; Dau, H.; Driess, M. Facile Formation of Nanostructured Manganese Oxide Films as High-Performance Catalysts for the Oxygen Evolution Reaction. *ChemSusChem* **2018**, *11*, 2554−2561.

(16) Menezes, P. W.; Walter, C.; Hausmann, J. N.; Beltrán-Suito, R.; Schlesiger, C.; Praetz, S.; Verchenko, Y. V.; Shevelkov, A. V.; Driess, M. Boosting Water Oxidation through In Situ Electroconversion of Manganese Gallide: An Intermetallic Precursor Approach. *Angew. Chemie Int. Ed.* **2019**, *58*, 16569−16574.

(17) Meng, Y.; Song, W.; Huang, H.; Ren, Z.; Chen, S.-Y.; Suib, S. L. Structure−Property Relationship of Bifunctional MnO_2 Nanostructures: Highly Efficient, Ultra-Stable Electrochemical Water Oxidation and Oxygen Reduction Reaction Catalysts Identified in Alkaline Media. *J. Am. Chem. Soc.* **2014**, *136*, 11452−11464.

(18) Takashima, T.; Hashimoto, K.; Nakamura, R. Mechanisms of PH-Dependent Activity for Water Oxidation to Molecular Oxygen by MnO_2 Electrocatalysts. *J. Am. Chem. Soc.* **2012**, *134*, 1519−1527.

(19) Bergmann, A.; Zaharieva, I.; Dau, H.; Strasser, P. Electrochemical Water Splitting by Layered and 3D Cross-Linked Manganese Oxides: Correlating Structural Motifs and Catalytic Activity. *Energy Environ. Sci.* **2013**, *6*, 2745−2755.

(20) Morgan Chan, Z.; Kitchaev, D. A.; Nelson Weker, J.; Schnedermann, C.; Lim, K.; Ceder, G.; Tumas, W.; Toney, M. F.; Nocera, D. G. Electrochemical Trapping of Metastable Mn^{3+} Ions for Activation of MnO_2 Oxygen Evolution Catalysts. *Proc. Natl. Acad. Sci. U. S. A.* **2018**, *115*, E5261−E5268.

(21) Indra, A.; Menezes, P. W.; Schuster, F.; Driess, M. Significant Role of Mn(III) Sites in e_g^1 Configuration in Manganese Oxide Catalysts for Efficient Artificial Water Oxidation. *J. Photochem. Photobiol. B Biol.* **2015**, *152*, 156−161.

(22) Zheng, W.; Liu, M.; Lee, L. Y. S. Best Practices in Using Foam-Type Electrodes for Electrocatalytic Performance Benchmark. *ACS Energy Lett.* **2020**, *5*, 3260−3264.

(23) Sahasrabudhe, A.; Dixit, H.; Majee, R.; Bhattacharyya, S. Value Added Transformation of Ubiquitous Substrates into Highly Efficient and Flexible Electrodes for Water Splitting. *Nat. Commun.* **2018**, *9*, 2014.

(24) Chaudhari, N. K.; Jin, H.; Kim, B.; Lee, K. Nanostructured Materials on 3D Nickel Foam as Electrocatalysts for Water Splitting. *Nanoscale* **2017**, *9*, 12231−12247.

(25) Lee, G.; Jeong, M.; Kim, H. R.; Kwon, M.; Baek, S.; Oh, S.; Lee, M.; Lee, D.; Joo, J. H. Controlled Electrophoretic Deposition Strategy of Binder-Free $CoFe_2O_4$ Nanoparticles as an Enhanced Electrocatalyst for the Oxygen Evolution Reaction. *ACS Appl. Mater. Interfaces* **2022**, *14*, 48598−48608.

(26) Wang, P.; Wang, B. Interface Engineering of Binder-Free Earth-Abundant Electrocatalysts for Efficient Advanced Energy Conversion. *ChemSusChem* **2020**, *13*, 4795−4811.

(27) Menezes, P. V.; Elnagar, M. M.; Al-Shakran, M.; Eckl, M. J.; Menezes, P. W.; Kibler, L. A.; Jacob, T. In-Liquid Plasma for Surface Engineering of Cu Electrodes with Incorporated SiO_2 Nanoparticles: From Micro to Nano. *Adv. Funct. Mater.* **2022**, *32*, 2107058.

(28) Klapkiv, M. D. State of an Electrolytic Plasma in the Process of Synthesis of Oxides Based on Aluminum. *Mater. Sci.* **1996**, *31*, 494−499.

(29) Rogov, A. B.; Yerokhin, A.; Matthews, A. The Role of Cathodic Current in Plasma Electrolytic Oxidation of Aluminum: Phenomenological Concepts of the "Soft Sparking" Mode. *Langmuir* **2017**, *33*, 11059−11069.

(30) Rogov, A. B.; Matthews, A.; Yerokhin, A. Relaxation Kinetics of Plasma Electrolytic Oxidation Coated Al Electrode: Insight into the Role of Negative Current. *J. Phys. Chem. C* **2020**, *124*, 23784−23797.

(31) Chauvin, J.; Judée, F.; Yousfi, M.; Vicendo, P.; Merbahi, N. Analysis of Reactive Oxygen and Nitrogen Species Generated in Three Liquid Media by Low Temperature Helium Plasma Jet. *Sci. Rep.* **2017**, *7*, 4562.

(32) Zaharieva, I.; Chernev, P.; Risch, M.; Klingan, K.; Kohlhoff, M.; Fischer, A.; Dau, H. Electrosynthesis, Functional, and Structural

Characterization of a Water-Oxidizing Manganese Oxide. *Energy Environ. Sci.* **2012**, *5*, 7081−7089.
(33) Huynh, M.; Bediako, D. K.; Liu, Y.; Nocera, D. G. Nucleation and Growth Mechanisms of an Electrodeposited Manganese Oxide Oxygen Evolution Catalyst. *J. Phys. Chem. C* **2014**, *118*, 17142−17152.
(34) Cheng, W.; Lindholm, J.; Holmboe, M.; Luong, N. T.; Shchukarev, A.; Ilton, E. S.; Hanna, K.; Boily, J.-F. Nanoscale Hydration in Layered Manganese Oxides. *Langmuir* **2021**, *37*, 666−674.
(35) McCrory, C. C. L.; Jung, S.; Peters, J. C.; Jaramillo, T. F. Benchmarking Heterogeneous Electrocatalysts for the Oxygen Evolution Reaction. *J. Am. Chem. Soc.* **2013**, *135*, 16977−16987.
(36) Huynh, M.; Bediako, D. K.; Nocera, D. G. A Functionally Stable Manganese Oxide Oxygen Evolution Catalyst in Acid. *J. Am. Chem. Soc.* **2014**, *136*, 6002−6010.
(37) Abrashev, M. V.; Chernev, P.; Kubella, P.; Mohammadi, M. R.; Pasquini, C.; Dau, H.; Zaharieva, I. Origin of the Heat-Induced Improvement of Catalytic Activity and Stability of MnO_x Electrocatalysts for Water Oxidation. *J. Mater. Chem. A* **2019**, *7*, 17022−17036.
(38) Vos, J. G.; Wezendonk, T. A.; Jeremiasse, A. W.; Koper, M. T. M. MnO_x /IrO_x as Selective Oxygen Evolution Electrocatalyst in Acidic Chloride Solution. *J. Am. Chem. Soc.* **2018**, *140*, 10270−10281.
(39) Niu, S.; Li, S.; Du, Y.; Han, X.; Xu, P. How to Reliably Report the Overpotential of an Electrocatalyst. *ACS Energy Lett.* **2020**, *5*, 1083−1087.
(40) Kang, Q.; Vernisse, L.; Remsing, R. C.; Thenuwara, A. C.; Shumlas, S. L.; McKendry, I. G.; Klein, M. L.; Borguet, E.; Zdilla, M. J.; Strongin, D. R. Effect of Interlayer Spacing on the Activity of Layered Manganese Oxide Bilayer Catalysts for the Oxygen Evolution Reaction. *J. Am. Chem. Soc.* **2017**, *139*, 1863−1870.
(41) Hausmann, J. N.; Mebs, S.; Laun, K.; Zebger, I.; Dau, H.; Menezes, P. W.; Driess, M. Understanding the Formation of Bulk- and Surface-Active Layered (Oxy)Hydroxides for Water Oxidation Starting from a Cobalt Selenite Precursor. *Energy Environ. Sci.* **2020**, *13*, 3607−3619.
(42) Ramírez, A.; Hillebrand, P.; Stellmach, D.; May, M. M.; Bogdanoff, P.; Fiechter, S. Evaluation of MnO_x, Mn_2O_3, and Mn_3O_4 Electrodeposited Films for the Oxygen Evolution Reaction of Water. *J. Phys. Chem. C* **2014**, *118*, 14073−14081.
(43) Wu, Z.-Y.; Ji, W.-B.; Hu, B.-C.; Liang, H.-W.; Xu, X.-X.; Yu, Z.-L.; Li, B.-Y.; Yu, S.-H. Partially Oxidized Ni Nanoparticles Supported on Ni-N Co-Doped Carbon Nanofibers as Bifunctional Electrocatalysts for Overall Water Splitting. *Nano Energy* **2018**, *51*, 286−293.
(44) Tarditi, A. M.; Barroso, N.; Galetti, A. E.; Arrúa, L. A.; Cornaglia, L.; Abello, M. C. XPS Study of the Surface Properties and Ni Particle Size Determination of Ni-Supported Catalysts. *Surf. Interface Anal.* **2014**, *46*, 521−529.
(45) Menezes, P. W.; Yao, S.; Beltrán-Suito, R.; Hausmann, J. N.; Menezes, P. V.; Driess, M. Facile Access to an Active γ-NiOOH Electrocatalyst for Durable Water Oxidation Derived From an Intermetallic Nickel Germanide Precursor. *Angew. Chemie Int. Ed.* **2021**, *60*, 4640−4647.
(46) Mondal, I.; Hausmann, J. N.; Vijaykumar, G.; Mebs, S.; Dau, H.; Driess, M.; Menezes, P. W. Nanostructured Intermetallic Nickel Silicide (Pre)Catalyst for Anodic Oxygen Evolution Reaction and Selective Dehydrogenation of Primary Amines. *Adv. Energy Mater.* **2022**, *12*, 2200269.
(47) Chen, D.; Ding, D.; Li, X.; Waller, G. H.; Xiong, X.; El-Sayed, M. A.; Liu, M. Probing the Charge Storage Mechanism of a Pseudocapacitive MnO_2 Electrode Using *in Operando* Raman Spectroscopy. *Chem. Mater.* **2015**, *27*, 6608−6619.
(48) Julien, C.; Massot, M.; Poinsignon, C. Lattice Vibrations of Manganese Oxides. *Spectrochim. Acta Part A Mol. Biomol. Spectrosc.* **2004**, *60*, 689−700.
(49) Julien, C.; Massot, M. Spectroscopic Studies of the Local Structure in Positive Electrodes for Lithium Batteries. *Phys. Chem. Chem. Phys.* **2002**, *4*, 4226−4235.
(50) Huang, J.; Li, Y.; Zhang, Y.; Rao, G.; Wu, C.; Hu, Y.; Wang, X.; Lu, R.; Li, Y.; Xiong, J. Identification of Key Reversible Intermediates in Self-Reconstructed Nickel-Based Hybrid Electrocatalysts for Oxygen Evolution. *Angew. Chemie Int. Ed.* **2019**, *58*, 17458−17464.
(51) Klingan, K.; Ringleb, F.; Zaharieva, I.; Heidkamp, J.; Chernev, P.; Gonzalez-Flores, D.; Risch, M.; Fischer, A.; Dau, H. Water Oxidation by Amorphous Cobalt-Based Oxides: Volume Activity and Proton Transfer to Electrolyte Bases. *ChemSusChem* **2014**, *7*, 1301−1310.
(52) Bediako, D. K.; Surendranath, Y.; Nocera, D. G. Mechanistic Studies of the Oxygen Evolution Reaction Mediated by a Nickel−Borate Thin Film Electrocatalyst. *J. Am. Chem. Soc.* **2013**, *135*, 3662−3674.
(53) Mosa, I. M.; Biswas, S.; El-Sawy, A. M.; Botu, V.; Guild, C.; Song, W.; Ramprasad, R.; Rusling, J. F.; Suib, S. L. Tunable Mesoporous Manganese Oxide for High Performance Oxygen Reduction and Evolution Reactions. *J. Mater. Chem. A* **2016**, *4*, 620−631.
(54) Hausmann, J. N.; Menezes, P. W. Effect of Surface-Adsorbed and Intercalated (Oxy)Anions on the Oxygen Evolution Reaction. *Angew. Chemie Int. Ed.* **2022**, *61*, e202207279.
(55) Yang, C.; Rousse, G.; Louise Svane, K.; Pearce, P. E.; Abakumov, A. M.; Deschamps, M.; Cibin, G.; Chadwick, A. V.; Dalla Corte, D. A.; Anton Hansen, H.; Vegge, T.; Tarascon, J.-M.; Grimaud, A. Cation Insertion to Break the Activity/Stability Relationship for Highly Active Oxygen Evolution Reaction Catalyst. *Nat. Commun.* **2020**, *11*, 1378.
(56) Liu, L.; Wang, Y.; Zhao, Y.; Wang, Y.; Zhang, Z.; Wu, T.; Qin, W.; Liu, S.; Jia, B.; Wu, H.; Zhang, D.; Qu, X.; Chhowalla, M.; Qin, M. Ultrahigh Pt-Mass-Activity Hydrogen Evolution Catalyst Electrodeposited from Bulk Pt. *Adv. Funct. Mater.* **2022**, *32*, 2112207.
(57) Chen, Z.; Yang, H.; Kang, Z.; Driess, M.; Menezes, P. W. The Pivotal Role of S-, P-, and F-Block Metals in Water Electrolysis: Status Quo and Perspectives. *Adv. Mater.* **2022**, *34*, 2108432.
(58) Hausmann, J. N.; Mebs, S.; Dau, H.; Driess, M.; Menezes, P. W. Oxygen Evolution Activity of Amorphous Cobalt Oxyhydroxides: Interconnecting Precatalyst Reconstruction, LongRange Order, Buffer-Binding, Morphology, Mass Transport, and Operation Temperature. *Adv. Mater.* **2022**, *34*, 2207494.
(59) Indra, A.; Menezes, P. W.; Zaharieva, I.; Baktash, E.; Pfrommer, J.; Schwarze, M.; Dau, H.; Driess, M. Active Mixed-Valent MnO_x Water Oxidation Catalysts through Partial Oxidation (Corrosion) of Nanostructured MnO Particles. *Angew. Chemie Int. Ed.* **2013**, *52*, 13206−13210.
(60) Li, R.; Xiang, K.; Peng, Z.; Zou, Y.; Wang, S. Recent Advances on Electrolysis for Simultaneous Generation of Valuable Chemicals at Both Anode and Cathode. *Adv. Energy Mater.* **2021**, *11*, 2102292.
(61) Bender, M. T.; Choi, K.-S. Electrochemical Dehydrogenation Pathways of Amines to Nitriles on NiOOH. *JACS Au* **2022**, *2*, 1169−1180.